Ultrafast energy- and momentum-resolved dynamics of magnetic correlations in the photo-doped Mott insulator Sr_2IrO_4

M. P. M. Dean[1]*[†], Y. Cao[1]*[†], X. Liu[2,3]*, S. Wall[4], D. Zhu[5], R. Mankowsky[6,7], V. Thampy[1], X. M. Chen[1], J. G. Vale[8], D. Casa[9], Jungho Kim[9], A. H. Said[9], P. Juhas[1], R. Alonso-Mori[5], J. M. Glownia[5], A. Robert[5], J. Robinson[5], M. Sikorski[5], S. Song[5], M. Kozina[5], H. Lemke[5], L. Patthey[10], S. Owada[11], T. Katayama[12], M. Yabashi[11], Yoshikazu Tanaka[11], T. Togashi[12], J. Liu[13], C. Rayan Serrao[14], B. J. Kim[15], L. Huber[16], C.-L. Chang[17], D. F. McMorrow[8], M. Först[6,7] and J. P. Hill[1]

Measuring how the magnetic correlations evolve in doped Mott insulators has greatly improved our understanding of the pseudogap, non-Fermi liquids and high-temperature superconductivity[1-4]. Recently, photo-excitation has been used to induce similarly exotic states transiently[5-7]. However, the lack of available probes of magnetic correlations in the time domain hinders our understanding of these photo-induced states and how they could be controlled. Here, we implement magnetic resonant inelastic X-ray scattering at a free-electron laser to directly determine the magnetic dynamics after photo-doping the Mott insulator Sr_2IrO_4. We find that the non-equilibrium state, 2 ps after the excitation, exhibits strongly suppressed long-range magnetic order, but hosts photo-carriers that induce strong, non-thermal magnetic correlations. These two-dimensional (2D) in-plane Néel correlations recover within a few picoseconds, whereas the three-dimensional (3D) long-range magnetic order restores on a fluence-dependent timescale of a few hundred picoseconds. The marked difference in these two timescales implies that the dimensionality of magnetic correlations is vital for our understanding of ultrafast magnetic dynamics.

In the layered perovskite Sr_2IrO_4, multiple interactions conspire to determine its electronic configuration. Strong spin–obit coupling splits the Ir $5d$ states to form a narrow electronic band that can be further split by the modest on-site Coulomb repulsion to generate an antiferromagnetic Mott insulating state with close structural and electronic analogies to the superconducting cuprates[2–4,8,9]. It has been well established that when a perturbation destroys magnetic order in a Mott insulator, the resulting new state frequently exhibits unusual properties[10]. For example, surface doping and Rh–Ir substitution in Sr_2IrO_4 have generated novel Fermi-arc and pseudogap behaviour[2–4], and some have argued that doped Sr_2IrO_4 might host high-temperature superconductivity[11,12]. In both cases, magnetic correlations were argued to play a critical role in the formation of these states. Photo-doping a Mott insulator using ultrafast lasers provides an alternative route to create transient versions of these exotic states, with the advantage that the resulting states are tunable and reversible. So far, however, there has been a lack of appropriate tools to probe the momentum and energy dependence of the electronic and magnetic correlations characterizing these ultrafast transient states.

Figure 1 illustrates our experimental approach. Sr_2IrO_4 was cooled to 110 K, well below its Néel ordering temperature of 240 K (ref. 13). Pump laser pulses with an energy of 620 meV (2 μm) drive carriers from the lower Hubbard band to the upper Hubbard band[14]. The transient magnetic response to this pump was characterized using a free-electron laser. X-ray photons were tuned to the Ir L_3 resonance to couple to the spin degree of freedom through the resonant magnetic X-ray scattering mechanism and photons scattered around 90° were measured as a function of momentum transfer, $\mathbf{Q}$, energy loss, E, and time delay, t. Further details are provided in the Methods.

Figure 2a,b plots the time and fluence dependence of the $(-3, -2, 28)$ magnetic Bragg peak intensity in Sr_2IrO_4, which is sensitive to the presence of 3D magnetic order. This intensity is measured by an area detector without energy analysis of the scattered photons. We find that fluences of $\gtrsim 5$ mJ cm^{-2} destroy the 3D magnetic order based on the criterion of having $\lesssim 10\%$ remnant

[1]Department of Condensed Matter Physics and Materials Science, Brookhaven National Laboratory, Upton, New York 11973, USA. [2]Beijing National Laboratory for Condensed Matter Physics and Institute of Physics, Chinese Academy of Sciences, Beijing 100190, China. [3]Collaborative Innovation Center of Quantum Matter, Beijing, China. [4]ICFO-Institut de Ciències Fotòniques, The Barcelona Institute of Science and Technology, 08860 Castelldefels (Barcelona), Spain. [5]Linac Coherent Light Source, SLAC National Accelerator Laboratory, Menlo Park, California 94025, USA. [6]Max Planck Institute for the Structure and Dynamics of Matter, D-22761 Hamburg, Germany. [7]Center for Free Electron Laser Science, D-22761 Hamburg, Germany. [8]London Centre for Nanotechnology and Department of Physics and Astronomy, University College London, London WC1E 6BT, UK. [9]Advanced Photon Source, Argonne National Laboratory, Argonne, Illinois 60439, USA. [10]SwissFEL, Paul Scherrer Institut, CH-5232 Villigen PSI, Switzerland. [11]RIKEN SPring-8 Center, Sayo, Hyogo 679-5148, Japan. [12]Japan Synchrotron Radiation Institute, 1-1-1 Kouto, Sayo-cho, Sayo-gun, Hyogo 679-5198, Japan. [13]Department of Physics & Astronomy, University of Tennessee, Knoxville, Tennessee 37996, USA. [14]Department of Electrical Engineering and Computer Sciences, University of California, Berkeley, California 94720, USA. [15]Max Planck Institute for Solid State Research, D-70569 Stuttgart, Germany. [16]Institute for Quantum Electronics, ETH Zurich, CH-8093 Zurich, Switzerland. [17]Zernike Institute for Advanced Materials, University of Groningen, Groningen, NL 9747AG, The Netherlands. [†]These authors contributed equally to this work. *e-mail: mdean@bnl.gov; ycao@bnl.gov; xliu@iphy.ac.cn
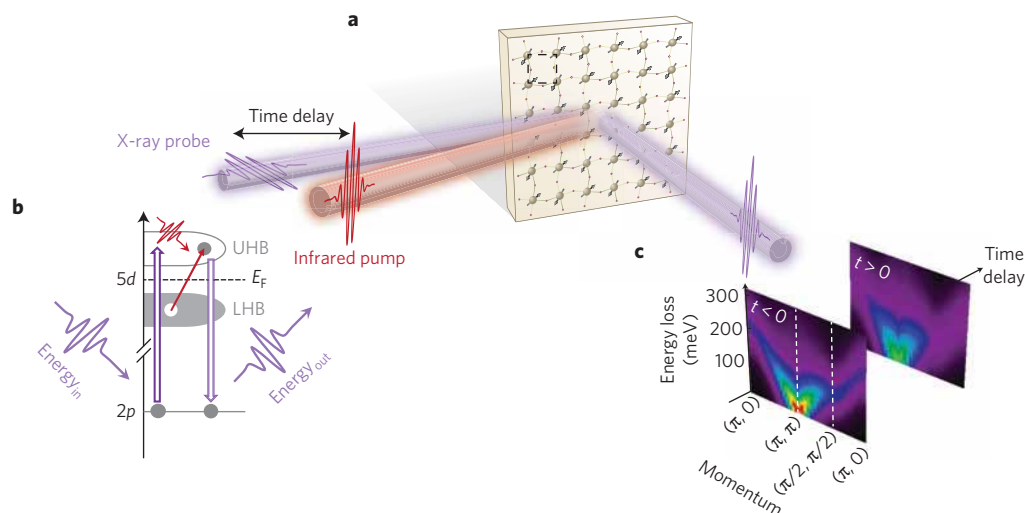
1

Figure 1 | Experimental configuration. a, The scattering set-up. The vertically polarized pump pulse (shown in red) is incident on the *ab*-face of Sr_2IrO_4. X-ray pulses from a free-electron laser (shown in purple) probe the resulting transient state. X-rays that are scattered close to 90° are either directly measured, to access the magnetic Bragg peak that probes the presence or absence of 3D magnetic order, or energy analysed to access the inelastic spectrum, which is particularly sensitive to the 2D magnetic correlations. The basic in-plane structural unit of Sr_2IrO_4 is outlined with a dotted black line. **b**, An illustration of the pump and probe processes. The 620 meV (2 μm) pump beam (in red) photo-dopes the sample, exciting an electron across the Fermi energy, E_F, from the lower Hubbard band (LHB) to the upper Hubbard band (UHB). Horizontally polarized 11.215 keV X-ray pulses from a free-electron laser (shown in purple) probe the resulting transient state. The incident X-ray pulses excite an Ir 2p core electron into the 5d valence band, to couple to the spin degree of freedom. The resulting emitted photon encodes the magnetic and orbital configuration of the transient state[23]. **c**, Illustration of the detection of X-rays as a function of energy loss, momentum transfer and time delay, encoding the time-dependent magnetic correlations in the transient state. The RIXS planes plot simple spin-wave calculations based on an increased thermal population of magnons after the pulse.
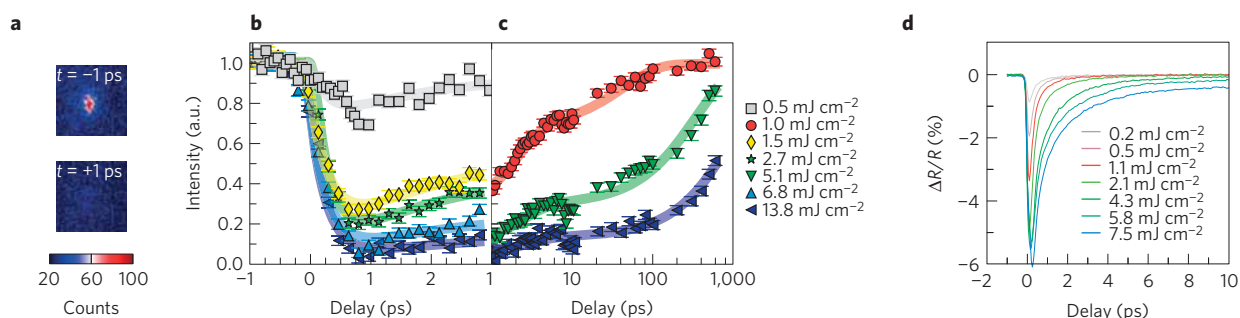

Figure 2 | Destruction and recovery of charge and 3D magnetic order in Sr_2IrO_4. a, Intensity of the $(−3, −2, 28)$ magnetic Bragg peak 1 ps before (top panel) and 1 ps after (bottom panel) excitation at 6.8 mJ cm$^{−2}$. **b,c**, Intensity of the magnetic Bragg peak as a function of probe delay focusing on the short (**b**) and long (**c**) timescales. The lines show the result of fitting the model, which incorporates one decay timescale and two recovery timescales. **d**, Relative change in the 800 nm optical reflectivity ($\Delta R/R$) of Sr_2IrO_4 after excitation with a 620 meV pump at different fluences. All data are taken at 110 K. Error bars represent the statistical uncertainty in the intensities assuming Poisson counting statistics.

intensity in the magnetic Bragg peak. This fluence corresponds to exciting a substantial fraction of all the lattice sites within the illuminated volume. Indeed, comparable fluences were also required to destroy long-range magnetic order in other strongly correlated materials, including manganites[15,16] and nickelates[17–19].

To characterize the charge response to the 620 meV (2 μm) pump excitation, we measured the optical reflectivity at 1.55 eV (800 nm) in Fig. 2d. The photo-carrier recombination is dominated by processes in the picosecond or sub-picosecond regime, far faster than the recovery of 3D magnetic order, suggesting that the charge and magnetic recovery processes are largely independent of one another.

A detailed understanding of ultrafast magnetic dynamics, beyond the presence or absence of 3D magnetic order, is severely hampered by limited experimental information regarding the short-range transient magnetic correlations. Other existing

techniques such as X-ray magnetic dichroism[20], Faraday rotation[21] and the magneto-optical Kerr effect[22] capture only 3D magnetic order. This Letter breaks new ground by energy analysing the scattered X-rays, that is, by performing the first ever time-resolved (tr) magnetic resonant inelastic X-ray scattering (RIXS) experiment. RIXS probes the magnetic quasiparticle spectrum itself[23,24]. This is a fundamental expression of the nature of the correlated electron state—as it is the spatial and temporal Fourier transform of the spin–spin correlation function and it encodes the interactions present in the magnetic Hamiltonian. In the present case of the 5d valence electron compound Sr_2IrO_4, the relevant X-ray L-edge is in the hard X-ray regime, allowing full access to reciprocal space. Such **Q**-space resolution is not available in the complementary technique of time-resolved two-magnon Raman scattering, owing to the fact that visible photons carry negligible momentum[25].
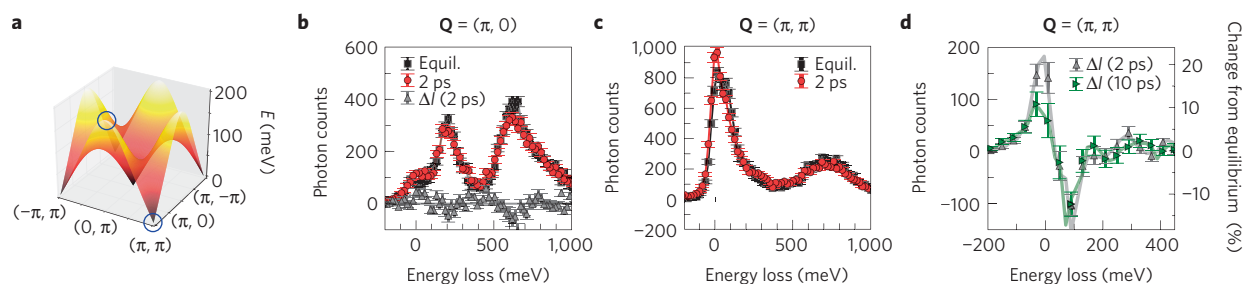
Figure 3 | 2D magnetic correlations before and after photo-excitation. a, Equilibrium state magnetic dispersions of Sr_2IrO_4 based on a spin-wave fit to measurements in ref. 9. The **Q**-vectors studied are outlined in blue. **b,c**, Time-resolved RIXS (tr-RIXS) spectra showing magnetic excitations (0–200 meV) and orbital excitations (~600 meV) in the equilibrium state 50 ps before photo-excitation (labelled Equil.) and 2 ps after photo-excitation at 6 mJ cm^{-2}. **b**, Spectra show that high-energy nearest-neighbour 2D magnetic correlations, as probed at **Q** = (π, 0), have completely recovered 2 ps after the pump. **c**, Spectra show that magnetic fluctuations at **Q** = (π, π) with relatively low energy arise from a small disturbance of the Néel order. **d**, Intensity difference spectra, ΔI, between the equilibrium state and the 2 ps transient state (from **c**) and between the equilibrium state and 10 ps. This shows a depletion of approximately 20% of the magnetic spectral weight around ~100 meV and additional spectral intensity appearing at very low energy. Poisson counting statistics were used to determine the error bars in **b**–**d**.

Figure 3 plots the RIXS energy loss spectra measured in Sr_2IrO_4 after photo-excitation at 6 mJ cm^{-2}, as compared to the unperturbed state 50 ps before excitation. The chosen pump fluence corresponds to what was required to destroy 3D magnetic order, as seen in Fig. 2a,b. The RIXS spectra show two dominant features, identified as magnon and orbital excitations[9,26,27], which we address in turn.

Orbital excitations appear in the RIXS spectra around 600 meV, and correspond to exciting a hole from the $J_{eff} = 1/2$ ground state orbital to the $J_{eff} = 3/2$ state[26,27]. The intensity of the orbital excitation is proportional to the $J_{eff} = 1/2 \rightarrow 3/2$ transition cross-section, and thus directly reflects the electron population in these orbitals. This excitation is different from the pump excitation at 620 meV in that the RIXS process involves two dipole transitions, so the process is allowed on a single site[23]. Given that a very similar amplitude of RIXS orbital excitations is seen before and after excitation, we infer that the majority, but not necessarily all, of the photo-excited carriers have decayed out of the $J_{eff} = 3/2$ orbital even in the 2 ps time window. Charge dynamics can also be measured indirectly through optical reflectivity. We see in Fig. 2d that the optical reflectivity at 6 mJ cm^{-2} is partially, but not fully, recovered at 2 ps delay. The residual reflectivity change probably results from a non-equilibrium charge distribution involving either spectral weight redistribution of the Hubbard bands or the population of in-gap charge states[28], but could also arise from transient structural modifications due to electron–phonon coupling.

The equilibrium excitation spectrum of undoped Sr_2IrO_4 can be accurately modelled in terms of magnons, or spin waves, that arise from Heisenberg spin–spin exchange interactions[9]. Figure 3a plots the magnetic dispersion from low energies at (π, π) to ~200 meV at (π, 0). Corresponding experimental RIXS spectra are plotted in Fig. 3b,c, with data shown both in the equilibrium (50 ps before the pump) and in the transient state after the pump. Despite the almost-complete destruction of the magnetic Bragg peak in the transient state, magnons are still observed at both **Q** points. Owing to the relatively weak c-axis exchange interaction in Sr_2IrO_4, the intensity, energy scale and dispersion of these magnons is most sensitive to the 2D Néel correlations between neighbouring spins[9]. This indicates that 2D correlations largely retain their Néel-like nature in the transient state 2 ps after the pump. The fact that the magnetic Bragg peak, as shown in Fig. 2a,b, is very strongly attenuated in the transient state is likely to be predominantly due to the destruction of inter-plane correlations along the c-axis. Looking at the RIXS difference spectra in detail, we see that the magnon at (π, 0) is identical before and after the pump. At (π, π), however, there is an appreciable change. This indicates that the high-energy ~200 meV correlations at (π, 0) are more robust than the lower-energy spin

wave at (π, π) that arises from a smaller disturbance of the Néel order. One interpretation of this observation is that the higher-energy magnons recover to their equilibrium configuration in much less than 2 ps, which could be owing to the fact that a higher-energy excitation can decay into lower-energy multi-particle excitations in a greater number of different ways than can the lower-energy magnons.

We now consider the magnetic excitation spectrum around (π, π) in more detail. Owing to the finite (± 0.5 Å^{-1}) momentum resolution of our spectrometer, the observed spectrum is the sum of the magnons with very low energy from precisely **Q** = (π, π), and of the magnons with slightly higher energy from closely neighbouring **Q** values. This leads to the asymmetric peak in Fig. 3c, which is further plotted as transient state difference spectra in Fig. 3d. We see that ~20% of the spectral intensity around ~100 meV has been depleted and additional very low energy spectral intensity appears, which recovers on a picosecond timescale. Thermal heating effects on 2D quantum antiferromagnets have been studied extensively and result in a uniform relative broadening of the magnons across the Brillouin zone[29,30]. Such broadening is not observed here, excluding a purely thermal explanation of our results. Given that we have established the presence of residual photo-excited carriers in the transient state, we suggest that these carriers are directly responsible for damping the magnetic correlations around ~100 meV and causing an apparent redistribution of the magnetic spectral weight to lower energy.

Having clarified the 2D correlations in the transient state, we reassess the behaviour of the 3D magnetic order presented in Fig. 2. Even in the few picosecond regime (Fig. 2b), a small amount of magnetic recovery is evident. However, full recovery takes somewhere between 100 and over 1,000 ps (Fig. 2c). We found that a minimal model for the magnetic intensity as a function of time, $I(t)$, required one decay timescale τ_{decay} and two recovery timescales—which, for reasons that we will explain later, are labelled τ_{2D} and τ_{3D}, where $\tau_{2D} < \tau_{3D}$

$$I(t) = I_0 \Big(\exp(-t/\tau_{decay}) + C \big[1 - \exp(-t/\tau_{2D}) \big] + (1-C) \big[1 - \exp(-t/\tau_{3D}) \big] \Big) \qquad (1)$$

This model was fitted to the magnetic Bragg peak intensity data in Fig. 2b,c. In a similar way, we fitted the recovery of the optical reflectivity, which also required two charge timescales, denoted T_{fast} and T_{slow}.

Figure 4 summarizes the magnetic and charge dynamics in Sr_2IrO_4 after laser excitation. 3D magnetic order decays in 0.30 ± 0.03 ps approximately independent of fluence (Fig. 4a),
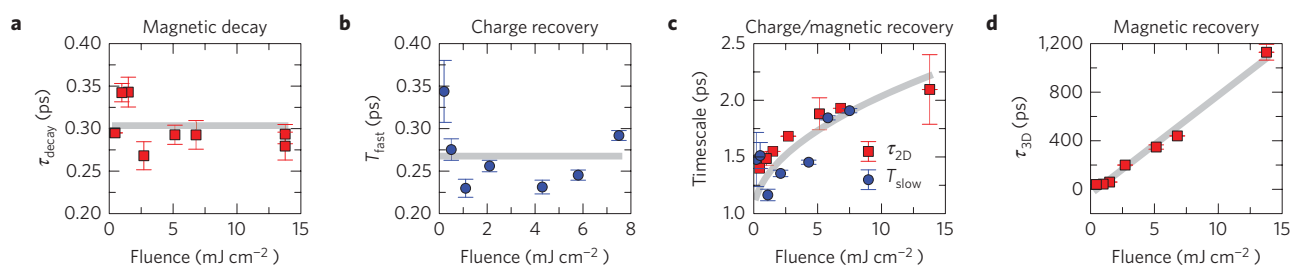
Figure 4 | Fluence dependence of the magnetic and charge dynamics timescales. a, Magnetic decay timescale τ_{decay}, showing that the magnetic decay happens in ≤ 0.3 ps, faster than the time resolution of the experiment. **b**, Fast charge recovery timescale T_{fast}. **c**, Timescales for the slow component of the charge recovery T_{slow} (blue) and the faster component of the magnetic recovery. From our RIXS data we know that the 2D magnetic correlations recover on a picosecond timescale, so owing to the similar timescale of this fitting parameter it is labelled τ_{2D} (red). These show strikingly similar magnitudes and fluence dependencies. **d**, τ_{3D} the slow magnetic recovery, which is assigned to the restoration of 3D magnetic order. Grey lines are guides to the eye and error bars are the standard deviation from the least-squares-fitting algorithm.

which is roughly equal to the jitter-limited time resolution of the experiment. This sets an upper limit on the timescale for the destruction of magnetic order in this system. The fast component of the charge recovery (Fig. 4b) is of a similar magnitude (0.27 ± 0.04 ps). In Fig. 4c, we plot the faster magnetic recovery timescale, which is ~1.7 ps and increases slowly with fluence. As discussed above, the 2D in-plane magnetic correlations recover on the picosecond timescale, so the lack of 3D magnetic order can be primarily attributed to the lack of coherence between the IrO_2 planes. Or, equivalently, after a few picoseconds there is a large population of low-energy long-wavelength magnons that, on average, preserve the 2D Néel correlations. Consequently, we attribute the fast timescale to 2D in-plane correlations and label it τ_{2D}. On a timescale of hundreds of picoseconds the 2D correlations are largely restored and the recovery is dominated by the restoration of 3D inter-plane correlations, leading us to assign the slower timescale to τ_{3D}. The marked difference in these timescales reflects the strong anisotropy in the magnetic interactions. Sr_2IrO_4 has very strong in-plane magnetic exchange $J_{\parallel} = 60$ meV and very weak inter-plane magnetic exchange, which some researchers have estimated to be as low as $J_{\perp} \approx 1\,\mu$eV (refs 9,27,31,32). τ_{3D} is also seen to be linear with fluence (Fig. 4d), increasing up to 1,130 ps at 13.8 mJ cm^{-2}. This implies that the recovery of the long-range magnetic order relies crucially on the dissipation of energy in the material, and is set by the timescale on which the low-energy long-wavelength magnons can dissipate their energy into the lattice degree of freedom, whereas τ_{2D} has a far weaker fluence dependence and seems to be related to a material property.

Time-resolved resonant X-ray scattering has provided a new window on the transient magnetic state in photo-doped Sr_2IrO_4. The 2D magnetic correlations we observe are non-thermal in nature and recover on a picosecond timescale denoted τ_{2D}. A striking similarity between τ_{2D} and the slower charge recovery timescale T_{slow} is seen in Fig. 4c. This may reflect the similar energy scale of the in-plane electronic hopping parameter, $t_{\parallel}$, and the magnetic exchange, $J_{\parallel}$, which are fundamentally linked in strongly correlated materials such as these through $J_{\parallel} \sim t_{\parallel}^2/U$, where U is the Coulomb repulsion. The behaviour of the long-range magnetic order, in contrast, depends on secondary processes, such as inter-plane magnetic coupling and the dissipation of the energy from the spins into other degrees of freedom.

This work shows that direct measurements of the 2D magnetic correlations are consequently crucial for a full understanding of magnetic dynamics in strongly correlated materials. With the continued improvement of free-electron lasers, tr-RIXS is set to play a crucial role in understanding how magnetic correlations dictate the properties of doped Mott insulators and how they can be effectively manipulated by light.

Methods

Methods and any associated references are available in the online version of the paper.

References

1. Scalapino, D. J. A common thread: the pairing interaction for unconventional superconductors. *Rev. Mod. Phys.* **84,** 1383–1417 (2012).
2. Kim, Y. *et al*. Fermi arcs in a doped pseudospin-1/2 Heisenberg antiferromagnet. *Science* **345,** 187–190 (2014).
3. Cao, Y. *et al*. Hallmarks of the Mott-metal crossover in the hole doped pseudospin-1/2 Mott insulator Sr_2IrO_4. *Nature Commun.* **7,** 11367 (2016).
4. de la Torre, A. *et al*. Collapse of the Mott gap and emergence of a nodal liquid in lightly doped Sr_2IrO_4. *Phys. Rev. Lett.* **115,** 176402 (2015).
5. Fausti, D. *et al*. Light-induced superconductivity in a stripe-ordered cuprate. *Science* **331,** 189–191 (2011).
6. Zhang, J. & Averitt, R. Dynamics and control in complex transition metal oxides. *Annu. Rev. Mater. Res.* **44,** 19–43 (2014).
7. Aoki, H. *et al*. Nonequilibrium dynamical mean-field theory and its applications. *Rev. Mod. Phys.* **86,** 779–837 (2014).
8. Kim, B. J. *et al*. Phase-sensitive observation of a spin-orbital Mott state in Sr_2IrO_4. *Science* **323,** 1329–1332 (2009).
9. Kim, J. *et al*. Magnetic excitation spectra of Sr_2IrO_4 probed by resonant inelastic X-ray scattering: establishing links to cuprate superconductors. *Phys. Rev. Lett.* **108,** 177003 (2012).
10. Lee, P. A., Nagaosa, N. & Wen, X.-G. Doping a Mott insulator: physics of high-temperature superconductivity. *Rev. Mod. Phys.* **78,** 17–85 (2006).
11. Wang, F. & Senthil, T. Twisted Hubbard model for Sr_2IrO_4: magnetism and possible high temperature superconductivity. *Phys. Rev. Lett.* **106,** 136402 (2011).
12. Yan, Y. J. *et al*. Electron-doped Sr_2IrO_4: an analogue of hole-doped cuprate superconductors demonstrated by scanning tunneling microscopy. *Phys. Rev. X* **5,** 041018 (2015).
13. Cao, G., Bolivar, J., McCall, S., Crow, J. E. & Guertin, R. P. Weak ferromagnetism, metal-to-nonmetal transition, and negative differential resistivity in single-crystal Sr_2IrO_4. *Phys. Rev. B* **57,** R11039–R11042 (1998).
14. Moon, S. J. *et al*. Electronic structures of layered perovskite Sr_2MO_4 ($M =$ Ru, Rh, and Ir). *Phys. Rev. B* **74,** 113104 (2006).
15. Ehrke, H. *et al*. Photoinduced melting of antiferromagnetic order in $La_{0.5}Sr_{1.5}MnO_4$ measured using ultrafast resonant soft X-ray diffraction. *Phys. Rev. Lett.* **106,** 217401 (2011).
16. Zhou, S. *et al*. Glass-like recovery of antiferromagnetic spin ordering in a photo-excited manganite $Pr_{0.7}Ca_{0.3}MnO_3$. *Sci. Rep.* **4,** 4050 (2014).
17. Chuang, Y. D. *et al*. Real-time manifestation of strongly coupled spin and charge order parameters in stripe-ordered $La_{1.75}Sr_{0.25}NiO_4$ nickelate crystals using time-resolved resonant X-ray diffraction. *Phys. Rev. Lett.* **110,** 127404 (2013).
18. Caviglia, A. D. *et al*. Photoinduced melting of magnetic order in the correlated electron insulator $NdNiO_3$. *Phys. Rev. B* **88,** 220401 (2013).
19. Lee, W.-S. *et al*. Phase fluctuations and the absence of topological defects in a photo-excited charge-ordered nickelate. *Nature Commun.* **3,** 838 (2012).

20. Boeglin, C. *et al*. Distinguishing the ultrafast dynamics of spin and orbital moments in solids. *Nature* **465**, 458–461 (2010).
21. Kampfrath, T. *et al*. Coherent terahertz control of antiferromagnetic spin waves. *Nature Photon.* **5**, 31–34 (2011).
22. Malinowski, G. *et al*. Control of speed and efficiency of ultrafast demagnetization by direct transfer of spin angular momentum. *Nature Phys.* **4**, 855–858 (2008).
23. Ament, L. J. P., vanVeenendaal, M., Devereaux, T. P., Hill, J. P. & van den Brink, J. Resonant inelastic X-ray scattering studies of elementary excitations. *Rev. Mod. Phys.* **83**, 705–767 (2011).
24. Dean, M. P. M. Insights into the high temperature superconducting cuprates from resonant inelastic X-ray scattering. *J. Magn. Magn. Mater.* **376**, 3–13 (2015).
25. Batignani, G. *et al*. Probing ultrafast photo-induced dynamics of the exchange energy in a Heisenberg antiferromagnet. *Nature Photon.* **9**, 506–510 (2015).
26. Ishii, K. *et al*. Momentum-resolved electronic excitations in the Mott insulator Sr_2IrO_4 studied by resonant inelastic X-ray scattering. *Phys. Rev. B* **83**, 115121 (2011).
27. Kim, J. *et al*. Excitonic quasiparticles in a spin–orbit Mott insulator. *Nature Commun.* **5**, 4453 (2014).
28. Okamoto, H. *et al*. Ultrafast charge dynamics in photoexcited Nd_2CuO_4 and La_2CuO_4 cuprate compounds investigated by femtosecond absorption spectroscopy. *Phys. Rev. B* **82**, 060513 (2010).
29. Manousakis, E. The spin-1/2 Heisenberg antiferromagnet on a square lattice and its application to the cuprous oxides. *Rev. Mod. Phys.* **63**, 1–62 (1991).
30. Rønnow, H. M. *et al*. Spin dynamics of the 2d spin $\frac{1}{2}$ quantum antiferromagnet copper deuteroformate tetradeuterate (CFTD). *Phys. Rev. Lett.* **87**, 037202 (2001).
31. Fujiyama, S. *et al*. Two-dimensional Heisenberg behavior of $J_{eff} = 1/2$ isospins in the paramagnetic state of the spin-orbital Mott insulator Sr_2IrO_4. *Phys. Rev. Lett.* **108**, 247212 (2012).
32. Vale, J. G. *et al*. Importance of XY anisotropy in Sr_2IrO_4 revealed by magnetic critical scattering experiments. *Phys. Rev. B* **92**, 020406 (2015).

Author contributions

J.P.H., X.L., M.P.M.D. and M.F. initiated and planned the project. M.P.M.D., Y.C., X.L., S.W., D.Z., R.M., V.T., X.M.C., J.G.V., D.C., J.K., A.H.S., P.J., R.A.-M., J.M.G., A.R., J.R., M.S., S.S., M.K., H.L., L.P., S.O., T.K., M.Y., Y.T., T.T., L.H., C.-L.C., D.F.M., M.F. and J.P.H. prepared for and performed the experiments. M.P.M.D., Y.C., X.L., S.W., M.F., D.F.M. and J.P.H. analysed and interpreted the data. J.L., C.R.S. and B.J.K. prepared the samples. M.P.M.D. and Y.C. wrote the paper with contributions from X.L., S.W., D.F.M., M.F. and J.P.H.

Additional information

Supplementary information is available in the online version of the paper. Reprints and permissions information is available online at www.nature.com/reprints. Correspondence and requests for materials should be addressed to M.P.M.D., Y.C. or X.L.

Competing financial interests

The authors declare no competing financial interests.

Methods

Samples. The magnetic Bragg peak measurements were performed on 200 nm epitaxial films of Sr_2IrO_4, to match the volume of Sr_2IrO_4 to the penetration depth of the pump, as the X-ray penetration depth is longer than the pump. The disappearance of the magnetic Bragg peak in Fig. 2a,b confirms that the whole probed volume is excited. The film was deposited on $SrTiO_3$ using pulsed laser deposition, as described in the Supplementary Information and ref. 33. Supplementary Figs 1 and 2 demonstrate good sample crystallinity and the lack of any detectable impurity phases. For RIXS, $\sim 1°$ grazing incidence X-rays were used to limit X-ray penetration depths to 80 nm on a bulk Sr_2IrO_4 crystal. Both samples have a c-axis surface normal. Reciprocal lattice notations are defined using the full unit cell with lattice constants $a = b = 5.51$ Å and $c = 25.7$ Å. The high-symmetry points in the in-plane Brillouin zone are defined in the reduced structural zone (which ignores the rotation of the IrO_6 octahedra) as in ref. 9. The zone centre, denoted (π, π) and the zone boundary denoted $(\pi, 0)$ correspond to $(1, 0, L)$ and $(0.5, 0.5, L)$, respectively, in the reciprocal lattice notation. In both experiments, the sample was cooled to about 110 K with a nitrogen cryostream, well below the Néel temperature of 240 K (ref. 13).

Optical pump. For both tr-REXS and tr-RIXS experiments, 100 fs pump pulses were generated at 620 meV (2 μm) using an optical parametric amplifier. The pulses were polarized vertically in the ab-plane of the sample and were incident at 13° with respect to the sample surface. The choice of pump energy follows previous optical conductivity measurements[14] and resonates between the upper and lower Hubbard bands.

The time-resolved resonant elastic X-ray scattering (tr-REXS) set-up. The tr-REXS experiment was performed at beamline 2 of the SPring-8 Angstrom Compact free-electron LAser (SACLA) with a 30 Hz pulse repetition rate. We adopted a horizontal scattering geometry, as seen in Fig. 1a, and tuned the X-ray energy to the peak in the Ir L_3-edge resonance around 11.215 keV. A multi-port charged coupled device (MPCCD) area detector was placed at $2\theta = 88.7°$ to observe the magnetic Bragg peak $(-3, -2, 28)$. This geometry is chosen to optimize the X-ray resonant magnetic scattering cross-section. We access the magnetic peak by rotating the sample around the vertical axis by $\phi = 12.8°$, with the infrared and X-ray photons in an approximately co-linear geometry. The detector was read out shot by shot and the signal was thresholded to suppress the background coming from X-ray fluorescence and electrical noise. The peak intensity was determined by binning the 2D MPCCD data into a 1D spectrum and fitting a Lorentzian lineshape with a uniform offset background. Each datapoint is the result of

summing 1,000–4,000 shots. Previous characterization of the beamline found that the time resolution of this experiment was jitter-limited to approximately 300 fs.

The minimal model for the fitting is outlined in the main text (equation (1)). This formula was convolved with a 100 fs Gaussian to account for the pump pulse width. The other major contribution to the effective time resolution was the X-ray pulse jitter of approximately 300 fs, because this is only an approximate value this was not included in the fit, rather this is taken as an upper limit on the decay time. Apart from this quantity, all parameters were varied to fit the data in the long-time-delay scans at 1.0, 2.7 and 13.8 mJ cm^{-2} fluence in Fig. 2c, and these fits were used to constrain τ_{3D} in fits of the short-time-delay data in Fig. 2b by interpolating the variation of τ_{3D} and C as a function of fluence. In this way, equation (1) provides an accurate parametrization of the recovery dynamics at all fluences studied.

The time-resolved resonant inelastic X-ray scattering (tr-RIXS) set-up. The tr-RIXS experiment was performed at the X-ray Pump Probe instrument[34] at the Linac Coherent Light Source (LCLS) with a 120 Hz repetition rate. We adopt a horizontal scattering plane, similar to the set-up in the tr-REXS experiment. The $(\pi, 0)$ and (π, π) data were measured at $(-3.5, -3.5, 24.1)$ and $(-4, -3, 23.9)$. Non-integer values of L were chosen to keep the X-ray incidence angle around 1°, as the RIXS spectrum is known to be essentially independent of L[9]. A Si (333) monochromator produced a 50 meV incident energy bandpass. The RIXS spectrometer is conceptually similar to that used at Sector 27 at the Advanced Photon Source. Scattered photons from the sample are reflected from a segmented spherical Si(8, 4, 4) analyser in a near-backscattering configuration and detected by a Princeton CCD. The sample, the analyser crystal, and the photodetector are placed on a Rowland circle with a radius of 1 m in the vertical plane. The total energy resolution of the tr-RIXS set-up was ~ 70 meV and the **Q** resolution was defined by the $\sim 6°$ angular acceptance of the analyser. RIXS spectra were collected in a stationary mode without moving the spectrometer, and the pixel-to-energy conversion was performed using well-established methods. The CCD was read out every 1,800 shots. Jitter and timing drift were the main contributions to the time resolution, which was on the order of 500 fs.

References

33. Rayan Serrao, C. *et al*. Epitaxy-distorted spin-orbit Mott insulator in Sr_2IrO_4 thin films. *Phys. Rev. B* **87,** 085121 (2013).
34. Chollet, M. *et al*. The X-ray pump-probe instrument at the LINAC coherent light source. *J. Synchrotron Radiat.* **22,** 503–507 (2015).